Monitoring Crop Seasonal Development under Biochar Treatment with Unmanned Aerial Vehicle (UAV)-based Multispectral Imagery

SAJA SALATTNA[1], JULIANE BENDIG[1], CHRISTINA KUCHENDORF[1],
CHRISTOPH JEDMOWSKI[1] & UWE RASCHER[1]

Abstract: Remote sensing data plays a crucial role in crop growth monitoring by characterizing the spatiotemporal variability of crop traits. In the context of climate-smart agriculture, the impact of biochar application in agroecosystems has received significant attention in recent years. However, despite the numerous studies examining the potential of biochar-facilitated fertilization on harvested crop yields and above-ground biomass production, monitoring of the impact of biochar treatments by remote sensing approaches on crop dynamics during the growing season has not been well addressed. Therefore, the main objective of this research was to provide a first case study to evaluate the potential of optical remote sensing to investigate the impact of biochar on crop growth. We used seasonal multispectral data acquired from an unmanned aerial vehicle (UAV) with high spatial resolution. In our case study, we used an off-the-shelf DJI Phantom 4 multispectral UAV system to monitor the seasonal development of spelt (Triticum aestivum ssp. spelta L.) in a biochar enrichment experiment. We here propose a straightforward data processing workflow based on an empirical line method to convert raw UAV data to normalized and comparable reflectance maps, which then were the bases for calculating various visible/near-infrared (VIS/NIR) vegetation indices. OSAVI was the best resolving index in relation to the actual yield, indicating equal to better spelt development over the biochar plots with a fertilizer level comparable to half and full conventional amount, compared to conventionally high fertilized controls.

1 Introduction

Global plant production faces the main challenge of sustainability under the constraint of the rapidly increasing population and the gradual depletion of natural resources (FRÓNA et al. 2019). In this context, reliable and timely information about the crop sown area becomes essential in developing management strategies in precision agriculture (RAMTEKE et al. 2020). Precision agriculture is a site-specific crop management approach that gathers, processes, and analyses spatial and temporal variability in soil, field, and crop parameters to support management decisions (SISHODIA et al. 2020). Remote sensing plays a crucial role in precision agriculture as it covers large areas rapidly and repeatedly, thus characterizing spatial and temporal crop traits. In addition to providing a synoptic view, remote sensing can provide structural information about vegetation health. As the spectral reflectance of the crop canopy changes with phenology (growth), stage and crop health, it can be measured and monitored by multispectral sensors (RAMTEKE et al. 2020) .

---

[1] Institute of Bio- and Geosciences: Plant Sciences (IBG-2),
Forschungszentrum Jülich GmbH, 52428 Jülich, Germany,
E-Mail: [s.salattna, j.bendig, c.kuchendorf, c.jedmowski, u.rascher]@fz-juelich.de

Satellite images have been widely adopted for crop monitoring due to the images' often sufficient spatial, spectral, and temporal resolution (LI et al. 2022; BLICKENSDÖRFER et al. 2022). Furthermore, high-resolution unmanned aerial vehicle (UAV)-based imagery has been used recently to address the data gap in satellite products suffering from cloud coverage and to address questions requiring centimeter-level spatial resolution(YAO et al. 2019).

In the context of mitigating climate change and adapting to the loss of soil fertility, there is a particular interest in assessing the impact of biochar-facilitated fertilizer application in agroecosystems (JEFFERY et al. 2011). Biochar is a black carbon-rich product obtained through the pyrolysis of various biomass feedstocks to intentionally amend the soil. Several studies have indicated that biochar application to soil can (i) improve soil fertility, (ii) enhance nutrient availability, (iii) increase soil water holding capacity and correlated growth and yield, (iv) increase microbial population and activities, and (v) reduce greenhouse gas emissions through carbon sequestration (TRUPIANO et al. 2017; BIEDERMAN & HARPOLE 2013). A commonly reported impact of biochar is the improvement of above-ground biomass productivity. Nevertheless, previous studies found that biochar could affect crop development only during the green-up phase, while the harvested crop yield could remain unaffected (HEIDARIAN DEHKORDI et al. 2020b).

Despite the growing literature investigating the effect of biochar on total crop productivity, the biochar effects on crop development over the growing season have received much less attention. Therefore, the spatio-temporal information provided by the UAV images can reveal variability in crop performance due to the presence of biochar within the agricultural soils. So far, HEIDARIAN DEHKORDI et al. (2020a) (2020b) have investigated the advanced perspectives of UAV (10 channel MicaSense RedEdge-M) remote sensing in combination with in-situ ground measurements of crop traits for monitoring the crops dynamic affected by century-old biochar enrichment in precision agriculture. To date, short-term biochar effects on plant systems using high-resolution UAV-based data at the canopy level have yet to be addressed.

The primary objective of this manuscript is to describe the ability to use the small-scale, high spatial-resolution UAV system to detect the differences between biochar fertilized fields and control fields and to investigate at which development stage those differences can be quantified or detected. Due to the high fertilization standard of the high-quality field, the expected impact of biochar-facilitated fertilization on crop growth may be low but possibly detectable using high spatial-resolution UAV data. The available imagery source was visible-near infrared multispectral data collected over one crop growth season. This study proposes a data processing workflow, from raw imagery to creating a reflectance map and extracting vegetation indices (VIs). These indices are used to answer the following question: Is it possible to detect the short-term impact of biochar treatments on spelt (*Triticum aestivum ssp. spelta* L.) crop performance at the canopy level using UAV-based crop traits?

2 Material and Methods

2.1 Site description

The study area was a farmer's field of approximately 21 hectares cultivated with spelt, located in Germany (latitude: 50° 58'55.1"N, and longitude: 6°25'50.4"E) (Figure 1). Spelt seeds were sown

in December 2022. The Muencheberg soil quality rating (SQR) of the area is >85, Colluvisol over Chernozem-parabraunerde. Spelt development was monitored during the experiment from the Booting stage to the senescence. The experimental treatment consisted of three biochar-enriched stripes with a diameter of 6 m along the field's length. Each stripe was treated with 1 ton/ha of terra preta biochar and 180 kg nitrogen/ha, 90 kg N/ha, and 40 kg N/ha for stripes T1, T2, and T3, respectively. Apart from these biochar-enriched stripes, the experimental field was exposed to homogeneous agricultural practices, and the soil was treated with organic minerals of 180 kg N/ha.
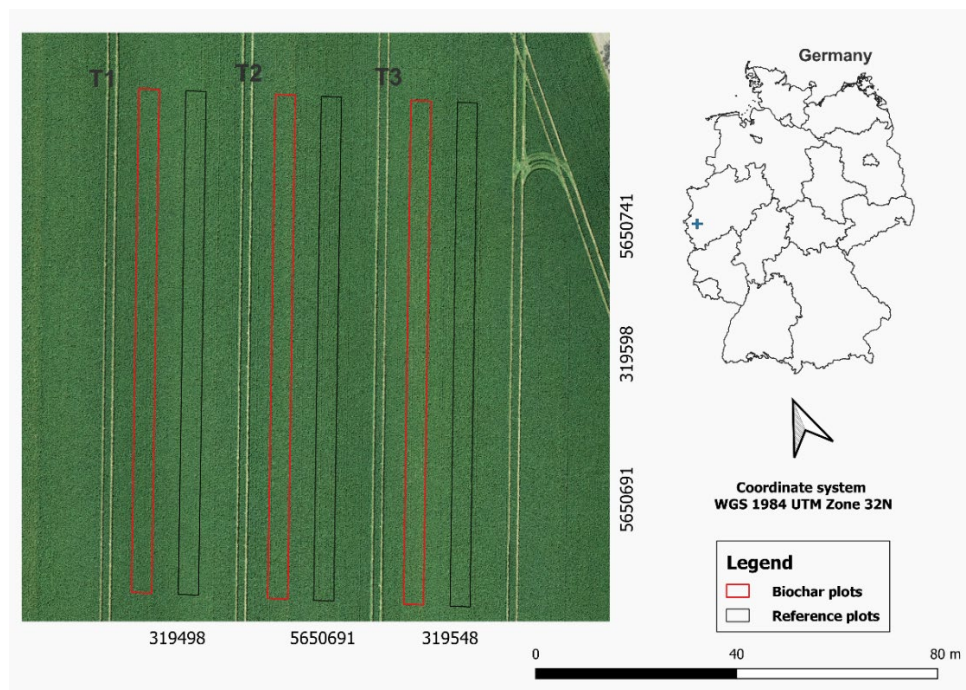

Fig. 1: Map of the experimental pairs (reference vs biochar plots) in the spelt field in Ameln-Titz, Germany. Background image corresponds to the Red-Green-Blue (RGB) orthomosaic captured by UAV on 02 June 2022

Three 3 ×100 m plots (red stripes in Fig. 1) were selected inside the biochar-enriched stripes, at least 1.5 m from the border of each stripe, to avoid gradient effects at the edge of the treatments. Subsequently, three plots of 3 ×100 m (black stripes in Fig. 1) were selected as reference soil areas within a distance of approximately 3 m from the biochar-enriched stripes to ensure comparable soil properties while preventing effects from mixing of biochar and reference soil particles. A set of ground control points (GCPs), consisting of five 0.3×0.3 m targets, were placed in the field for geo-referencing UAV images. GCP coordinates were measured with a real-time kinematic (RTK) global navigation satellite system (GNSS) (Hiper VR, Topcon Positioning Systems, Inc., Tokyo, Japan) with an overall accuracy of 0.01 m.

2.2   Unmanned Aerial Vehicle (UAV) data acquisition

A multispectral remote sensing dataset was acquired during the 2022 growing season using the multispectral camera mounted on the DJI Phantom 4 Multispectral (P4M). The P4M camera has six bands, including one RGB sensor and five monochrome sensors capturing blue (450 nm central

wavelength), green (560 nm), red (650 nm), red-edge (730 nm), and near-infrared (840 nm). Each spectral sensor has a global shutter and 1600×1300 pixels image resolution. In addition, the P4M is equipped with a band-by-band incident light sensor, which allows the irradiance measurement for each band during flight. The UAV was flown at 50 m above ground level (AGL) with an airspeed of 4.25 ms^{-1}. The forward and side image overlaps were 75% and 65%, resulting in a ground sampling distance (GSD) of 0.035 m. During data collection, six flights were performed between May and July 2022 in clear sky conditions and between 12:00 to 15:00 h local time. For each flight, a set of Lambertian reference panels with known hemispherical-conical reflectance factors was placed next to the field and recorded at flight altitude to enable the generation of reflectance maps in the postprocessing.

2.3 UAV-data preprocessing

2.3.1 Processing workflow

The data processing workflow, including data processing and vegetation indices extraction, is illustrated in Figure 2. First, the individual images were corrected for vignetting effect (section 2.3.2). Then, raw digital numbers (DNs) were corrected for sensor gain and exposure time yielding normalized-DN values (section 2.3.3). These two steps were performed on the individual images using an in-house developed python code. The corrected images were processed using the Metashape processing workflow (Agisoft LLC, St. Petersburg, Russia) that included GCPs for georeferencing orthomosaics as final products. The empirical line method (ELM) was applied for atmospheric correction and to create reflectance maps using a python code (section 2.3.4). Several vegetation indices were then calculated from the reflectance maps using the raster calculator tool in QGIS (section 2.4). In addition, a mask was applied to the vegetation indices maps in QGIS to exclude soil pixels before conducting the statistical tests to examine the difference between the reference and biochar plots (2.5).
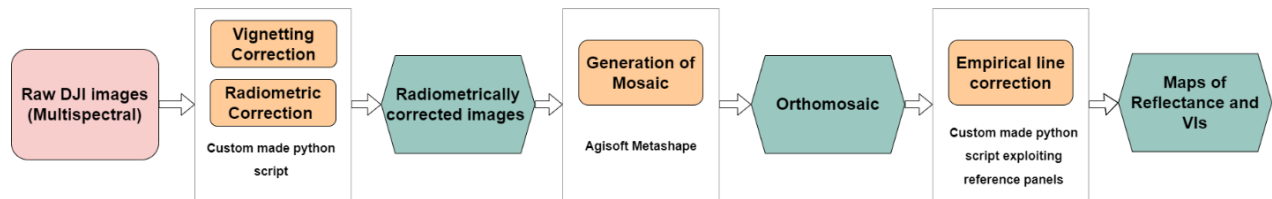

Fig. 2:   Overall multispectral UAV-image processing workflow

2.3.2 Vignetting correction

Vignetting is the effect of the radial falloff in pixel values, which results in darker areas near the edges of images (Goldman 2010). The vignetting effect, V(x, y), is typically modeled as a high-order polynomial (Equation 2). It assumes zero vignetting, $V(x_v, y_v) = 1$, at the image center:

$$r = \sqrt{(x - x_v)^2 + (y - y_v)^2} \qquad (1)$$

$$V(x, y) = 1 + \alpha_1 r + \alpha_2 r^2 + \alpha_3 r^3 + \alpha_4 r^4 + \alpha_5 r^5 + \alpha_6 r^6 \qquad (2)$$

Where r is the distance of the pixel (x, y) from the center of the vignette (x_v, y_v), which can be obtained by (Equation 2), matrix α shows the polynomial coefficients for the vignetting correction, which can be found in the EXIF/XMP metadata of the images.

The corrected image intensity ($I_{corrected}$) is calculated from the original image intensity I (x, y) using Equation (3):

$$I_{corrected}(x,y) = [I(x,y) - BL(x,y)] \times V(x,y) \qquad (3)$$

Where BL(x, y) is the normalized black level value, which can be found in EXIF/XMP metadata.

2.3.3 Radiometric correction

The radiometric correction is a crucial step in the processing flow. When an image is captured, raw data are stored as DNs, representing the radiant energy received by each pixel. During radiometric calibration, DNs are converted to radiance and usually later top of canopy reflectance to enable comparisons between datasets acquired under differing light conditions or with different sensors (MINAŘÍK et al. 2019). Radiance in absolute physical units cannot be calculated for DJI multispectral images as the sensor is not radiometrically calibrated by the manufacturer. Instead, normalized DNs are calculated using Equation 4, as described in Multispectral Image Processing Guide provided by DJI (DJI 2020):

$$DN_{corrected} = \frac{I_{corrected} \times 1_e{}^6}{sensor\ gain\ \times camera\ exposure\ time} \qquad (4)$$

where sensor gain and the camera exposure time can be found in XMP/EXIF metadata of each image, and $1_e{}^6$ is used to convert the exposure time from microseconds to seconds.

2.3.4 Mosaic generation

The individual images, corrected as described in sections 2.3.2 and 2.3.3, were imported into Agisoft Metashape to automate the image post-processing, recognize the characteristics of the used multispectral camera, and make the necessary geometric corrections (e.g., lens distortion). As the next step, the GPS metadata of the GCPs were used for geo-positioning and photogrammetric reconstruction, and finally, the software generated the orthomosaic and digital surface model.

2.3.5 Reflectance

ELM is commonly used for atmospheric correction and for generating surface reflectance data. The method assumes a linear relationship between DNs or radiance values in an image and surface reflectance (SMITH & MILTON 1999). Therefore, one or more reflectance calibration panels of known reflectance and Lambertian properties must be visible in the aerial imagery to apply the method. The UAV data for this study was acquired simultaneously with nine standard reflectance panels (2%, 3%,4 %,5%, 6%, 12%, 24%, 40% and 63%). First, the reference panel ROIs were manually extracted from the central part of each panel in the orthomosaic, for every flight, in QGIS. Then, the reference panel measurements were obtained band by band using a python script,

due to a displacement between the bands in the DJI P4 multispectral imageries. A mask was also applied for each orthomosaic within the python script to mask out the saturated panels for each spectral band. Then , ELM was applied to the orthomosaic to create a reflectance map as described in (CHAKHVASHVILI et al. 2021).

2.3.6 Calculation of Multispectral vegetation indices

Vegetation indices s allow monitoring spectral changes related to, e.g., crop structure, above-ground biomass, crop health, and weed presence (CUARAN & LEON 2021). The normalized difference vegetation index (NDVI) is a good indicator for green biomass, with the well-known shortcomings of saturating in closed canopies and being influenced by soil reflectance. The enhanced vegetation index (EVI) was proposed to address this issue by adjusting for atmospheric conditions and canopy background noise using a blue band. The normalized difference red edge index (NDRE) was identified as a good proxy of nitrogen concentration. The chlorophyll index red (CI-red) and the simplified canopy chlorophyll content index (s-CCCI) are often used for evaluating canopy chlorophyll and nitrogen content. The optimized soil-adjusted vegetation index (OSAVI) and chlorophyll vegetation index (CVI) are indicative of leaf chlorophyll content. Formulae and references are displayed in Tab. 1.

Tab. 1: Multispectral vegetation indices calculated in this study

Index		Formulae	Reference
Normalized Difference Vegetation Index	NDVI	(NIR – Red) / (NIR + Red)	(BUSCHMANN & NAGEL 1993)
Normalized Difference Red Edge	NDRE	(NIR -RE) / (NIR + RedEdge)	(GITELSON & MERZLYAK 1994)
Enhance Vegetation Index	EVI	2.5 * [(NIR – Red) / (NIR + 6*Red – 7.1*Blue + 1)]	(ZHANG et al. 2006)
Optimized soil adjusted VI	OSAVI	1.16 (NIR – Red)/ (NIR + Red+.16)	(LIMA-CUETO et al. 2019)
Chlorophyll vegetation index	CVI	(NIR/Green) * (Red/Green)	(VINCINI et al. 2008)
Chlorophyll index red	CI-red	(NIR/Red) - 1	(GITELSON et al. 2003)
Simplified canopy chlorophyll content index	s-CCCI	NDRE/ NDVI	(FITZGERALD et al. 2006)

2.4 Statistical Analysis

Analysis of Variance (ANOVA) and Tukey-Kramer post hoc test (NANDA et al. 2021) were used to determine whether the contrasts between the mappings of reference and biochar plots were statistically significant. As expected, a significant difference was found at a very high level due to the high number of samples (n) and, therefore, low variance. Since this is inconclusive, Cohen's D as a standardized mean difference (AARTS et al. 2013) was used to estimate the distance between means as effect size. Since the data distribution of pixel values can be fitted with a gaussian function, a comparison of means with a factor is possible. Therefore, peaks of the overlapping Gaussian functions can be distinguished, indicating that the underlying images (treatments) are from different datasets and differ to a certain degree. Cohen's D (as effect size) and the means ± standard deviation (SD) are discussed in this manuscript as means of differentiation and possibly

magnitude or contrast in VI representation.The effect size is interpreted using the classification developed by COHEN (1988), which is presented in Tab. 2:

Tab. 2: Cohen's D effect size classification

Effect size (D)	Interpretation
$0{,}00 \leq D < 0{,}20$	Ignored
$0{,}20 \leq D < 0{,}50$	low
$0{,}50 \leq D < 0{,}80$	Medium
$0{,}80 \leq D < 1{,}00$	Strong
$1{,}00 \leq D$	Very Strong

3   Results and Discussion

Figure 3 exemplarily illustrates the time series for OSAVI. The data collection started in May when the spelt was between the booting phase and inflorescence emergence. The mean of the observed areas (T1-R3) relates to plant health through chlorophyll content, which is, during the vegetative phase, a sign of healthy, well-supplied, and growing plants. The highest values are expected just before flowering, and mean values decline towards senescence.
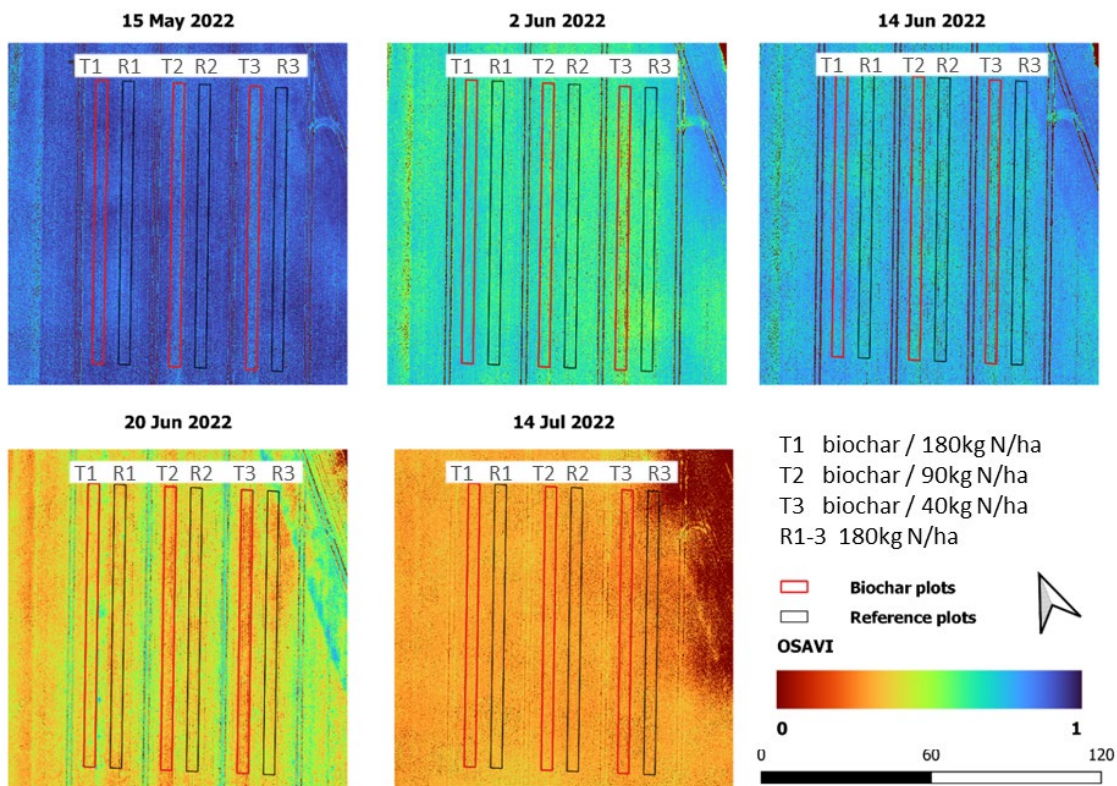

Fig. 3:   Optimized soil adjusted vegetation index (OSAVI) time series; the boxes are the areas with biochar-fertilizer treatments as shown in Fig. 1. Colouring shows the seasonal dynamic in mean pixel values of this index

On the second measurement day (2nd June), OSAVI was lower compared to 15th May and rose again on 14th June, which is also apparent in the boxplot in Fig. 4. This response is likely related

to weather conditions (not shown), where the field experienced a dry and slightly too warm May with insufficient rain and some colder days with possible light stress towards 2nd June, followed by warm and moist enough conditions until 14th June. This response could be seen as a recovery on 14th June from a short stress period; from around 14th June on, there were the only short phases of optimal growing conditions in an otherwise too dry and warm growing season, though that fit well with spelt senescence timing. From 14th June onwards, OSAVI constantly decreased due to the onset of senescence until 14th July, one day before the harvest.

The mean OSAVI value of the biochar treatment 1 plot (red box) was higher than in the adjacent reference plot (grey box) (same order as in Fig. 3) at each acquisition date except on 14th July, when the mean OSAVI was 0.3 for both reference and biochar plots (Fig. 4). Cohen's D showed that the difference was nearly negligible on all the dates with a D value less than 0.2, except for 2nd and 29th June, which have a medium and low effect with D = 0.54, and 0.37, respectively. For treatment 2, reported Cohen's D effects compared to the references except for 15th May and 29th June could be mostly ignored. In contrast, Cohen's D indicated a medium effect between treatment 3 and its adjacent reference on 15th May, 2nd and 29th June, and a medium to very strong effect toward treatment 1 with D values of .71, 1.18, and 1.19, respectively. These numbers indicate that the spelt is denser and healthier in treatment 1 compared to the reference plots and treatment 2. Both performed better than treatment 3; an effect was visible by eye at harvest in July.
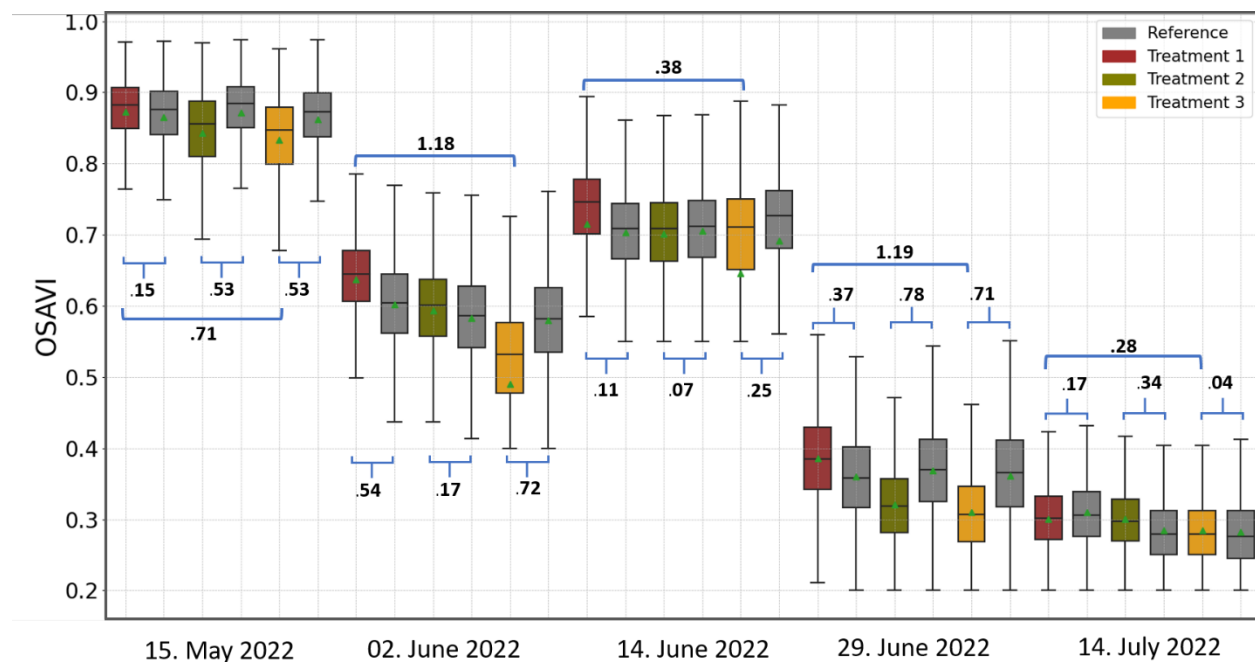

Fig. 4:   Comparison of the optimized soil adjusted vegetation index (OSAVI) of the three biochar stripes versus the three reference stripes for each acquisition date. Whiskers show highest and lowest values respectively, dividing line is the median, green triangle the mean. Brackets indicate comparisons between treatments, with respective Cohen's D value

Graphs of other examined multispectral vegetation indices are not presented here but data can be found in Tab. 3 and 4. Biochar treatment effects became visible in all VIs. However, those effects were negligible on 15th May for nearly all the VIs except EVI, which showed a medium to strong

effect, and OSAVI indicated a Medium effect. On 2nd, 14th, and 29th June, NDVI, EVI, NDRE, and OSAVI exhibited medium to very strong impact with a D value ranging up to 0.5 and higher.

Tab. 3: Mean vegetation index values and maximum distance between means (%)
for the biochar and reference plots during the growing season 2022

		15.05.2022	02.06.2022	14.06.2022	29.06.2022	14.07.2022
NDVI	total mean ±STD	0.91 ±0.04	0.67 ±0.08	0.79 ±0.05	0.41 ±0.09	0.3 ±0.05
	max dist. btw. means [%]	1.70%	12.8%	3.13%	17.9%	11.2%
EVI	total mean ±STD	0.56 ±0.1	0.63 ±0.13	0.73 ±0.1	0.27 ±0.07	0.29 ±0.05
	max diff. btw. means [%]	16.7%	24.0%	6.58%	22.0%	4.95%
OSAVI	total mean ±STD	0.86 ±0.06	0.58 ±0.1	0.69 ±0.13	0.35 ±0.07	0.29 ±0.05
	max diff. btw. means [%]	4.48%	22.9%	9.67%	19.7%	5.15%
NDRE	total mean ±STD	0.39 ±0.05	0.17 ±0.05	0.2 ±0.06	0.22 ±0.04	0.16 ±0.04
	max diff. btw. means [%]	7.14%	24.7%	20.9%	9.83%	6.58%
Clred	total mean ±STD	25.3 ±9.49	4.23 ±1.47	7.97 ±3.17	1.43 ±0.57	0.96 ±0.29
	max diff. btw. means [%]	14.7%	33.0%	17.1%	29.4%	15.8%
CVI	total mean ±STD	6.88 ±2.39	3.34 ±1.01	9.01 ±1.97	7.51 ±2.25	4.28 ±1.18
	max diff. btw. means [%]	15.9%	12.6%	14.8%	5.54%	15.9%
s-CCCI	total mean ±STD	0.42 ±0.05	0.25 ±0.07	0.26 ±0.06	0.54 ±0.11	0.53 ±0.13
	max diff. btw. means [%]	8.45%	16.5%	17.5%	13.7%	6.99%

Overall, the findings correlate well with fertilization management, where treatment 1 received the same amount of conventional nitrogen fertilizer as was used for the reference under standard cultivation. Treatment 2 received half the amount of fertilizer, and treatment 3 received no additional fertilization except the replacement of formerly depleted N on the field, resulting in 22% less N than the references. As for the crop yield, the farmer reported that treatment 1 was about 5% higher than the reference yield, and treatment 2 was like the reference despite having received half the fertilization. However, treatment 3 yield was 20% less than the references (direct communication).

All examined vegetation indices showed negligible to low difference between biochar and reference plots on the 14th July. OSAVI and EVI performing best in the vegetative phase. CVI showed overall large variances and is likely not recommended for detecting the effects of biochar in a homogeneous grassy cereal canopy. For comparisons between VIs, the ability to resolve differences between treatments, expressed by a wide range of values, and resolution, relating to the change of mean over the whole season should be considered. It should be noted that the approach of effect-size-based evaluation, essentially comparable to an arbitrary calibration of colour values (via Cohen's D), appears to work well in this case and correlates with the actual productivity and observations.

Tab. 4: The magnitude of difference/distance between means by Cohen's D of the vegetation indices comparing the biochar-treated and reference plots; strong and very strong effects **bold (D > .80)**; T1-T3, the overall largest difference as expected between highly and lower-than-conventional fertilization, measured by final yield as well as most indices, highlighted in grey. Not all comparisons (15 overall) shown. Underscored values correlate with the maximum distance ([%], see table 2) for the respective index on that acquisition

Date/ Index		15 May 2022	02 Jun 2022	14 Jun 2022	29 Jun 2022	14 Jul 2022
NDVI	T1 - T2	0.05	0.62	0.54	0.77	0.09
	T1 - T3	0.17	**1.44**	0.46	**0.98**	0.41
	T2- T3	0.21	**0.84**	0.09	0.19	0.32
	T1 - R1	0.02	0.53	0.52	0.26	0.01
	T2 - R2	0.2	0.2	0.1	0.64	0.1
	T3 - R3	0.36	0.64	0.26	0.77	0.29
EVI	T1 - T2	**0.96**	0.63	0.49	**0.97**	0.13
	T1 - T3	**1.17**	**1.48**	0.32	**1.06**	0.26
	T2- T3	0.19	0.76	0.16	0.11	0.14
	T1 - R1	0.21	0.66	0.48	0.4	0.02
	T2 - R2	**0.86**	0.25	0.09	0.74	0.11
	T3 - R3	0.73	0.42	0.11	**0.81**	0.02
OSAVI	T1 - T2	0.55	0.67	0.12	**1.02**	0.01
	T1 - T3	0.71	**1.18**	0.38	**1.19**	0.28
	T2 - T3	0.16	**0.84**	0.35	0.2	0.34
	T1 - R1	0.15	0.54	0.11	0.37	0.17
	T2 - R2	0.53	0.17	0.07	0.78	0.34
	T3 - R3	0.51	0.72	0.25	0.71	0.04
NDRE	T1 - T2	0.25	0.72	**0.81**	0.04	0.08
	T1 - T3	0.58	**1.01**	**0.91**	0.23	0.1
	T2 - T3	0.29	0.28	0.09	0.26	0.02
	T1 - R1	0.11	0.3	0.29	0.1	0.08
	T2 - R2	0.24	0.24	0.4	0.27	0.05
	T3 - R3	0.38	0.62	0.51	0.15	0.07
Clred	T1 - T2	0.09	0.58	0.52	0.73	0.08
	T1 - T3	0.15	**1.31**	0.42	**0.92**	0.31
	T2- T3	0.26	0.78	0.11	0.18	0.22
	T1 - R1	0.02	0.53	0.48	0.27	0.03
	T2 - R2	0.19	0.18	0.12	0.6	0.08
	T3 - R3	0.36	0.6	0.29	0.73	0.22
CVI	T1 - T2	0.33	0.19	0.62	0.13	0.06
	T1 - T3	0.3	0.07	0.67	0.19	0.42
	T2 - T3	0.03	0.11	0.06	0.06	0.48
	T1 - R1	0.06	0.26	0.08	0.19	0.2
	T2 - R2	0.18	0.33	0.57	0.06	0.07
	T3 - R3	0.1	0.17	0.4	0.14	0.05
s-CCCI	T1 - T2	0.44	0.66	0.64	0.78	0.05
	T1 - T3	0.73	0.68	**0.83**	0.76	0.22
	T2 - T3	0.27	0.01	0.16	0	0.17
	T1 - R1	0.13	0.14	0.09	0.37	0.11
	T2 - R2	0.3	0.38	0.4	0.34	0.01
	T3 - R3	0.42	0.53	0.46	0.65	0.06

However, this approach may not be generalizable since there are pitfalls in the statistical applicability, which may not have appeared here due to high homogeneity, but which nevertheless must be considered. An example is the high number of degrees of freedom with the extremely high

n. It is not necessarily a true high n since other influences besides fertilization cannot be ruled out completely. In an extreme case, one could regard this experiment as one random sample with n=6 and 5 degrees of freedom. This observation could be alleviated by, e.g., bootstrapping and increasing the number of observations artificially, which allows for a post-experiment randomization to see if the initial observations still hold. Such an analysis would enable analysing how small an experimental area could be to rule out side effects while still being valid, which is advisable for future experiments.

In conclusion, differentiating short-term biochar treatments via Cohen's D works for VIs derived from multispectral, high spatial resolution UAV images. The biochar treatment showed the most indicative impact on spelt crop during the inflorescence emergence. In direct comparisons, vegetation indices, especially OSAVI, enable evaluating plant status and possibly forecasting yield locally, which may help to optimize soil pre-treatment or fertilization. However, comparisons with ground truth data from yield and scoring plants throughout the season should be performed to solidify the findings. In addition, the minimum plot size for differentiation of biochar-facilitated fertilization should be determined in the future.

4   Acknowledgment

5   References

AARTS, S., VAN DEN AKKER, M. & WINKENS, B., 2013: The importance of effect sizes (1381-4788), 61-64, https://oi.org/10.3109/13814788.2013.818655.

BLICKENSDÖRFER, L., SCHWIEDER, M., PFLUGMACHER, D., NENDEL, C., ERASMI, S. & HOSTERT, P., 2022: Mapping of crop types and crop sequences with combined time series of Sentinel-1, Sentinel-2 and Landsat 8 data for Germany. Remote Sensing of Environment, **269**, 112831, https://oi.org/10.1016/j.rse.2021.112831.

BUSCHMANN, C. & NAGEL, E., 1993: In vivo spectroscopy and internal optics of leaves as basis for remote sensing of vegetation. International Journal of Remote Sensing, **14**(4), 711-722, https://oi.org/10.1080/01431169308904370.

CHAKHVASHVILI, E., SIEGMANN, B., BENDIG, J. & RASCHER, U., 2021: Comparison of Reflectance Calibration Workflows for a UAV-Mounted Multi-Camera Array System, 8225-8228, https://oi.org/10.1109/IGARSS47720.2021.9555143.

COHEN, J., 1988: Statistical Power Analysis for the Behavioral Sciences. 2nd ed. New York: NY: Routledge Academic.

CUARAN, J. & LEON, J., 2021: Crop Monitoring using Unmanned Aerial Vehicles: A Review. AG (Of), https://oi.org/10.18805/ag.R-180.

DJI, 2020: P4 Multispectral Image Processing Guide. https://dl.djicdn.com/downloads/p4-multispectral/20200717/P4_Multispectral_Image_Processing_Guide_EN.pdf, last access 05.02.2023.

FITZGERALD, G. J., RODRIGUEZ, D., CHRISTENSEN, L. K., BELFORD, R., SADRAS, V. O. & CLARKE, T. R., 2006: Spectral and thermal sensing for nitrogen and water status in rainfed and irrigated wheat environments. Precision Agric, **7**(4), 233-248, https://oi.org/10.1007/s11119-006-9011-z.

FRÓNA, D., SZENDERÁK, J. & HARANGI-RÁKOS, M., 2019: The Challenge of Feeding the World **11**(20), 5816, https://oi.org/https://doi.org/10.3390/su11205816.

GITELSON, A. & MERZLYAK, M. N., 1994: Spectral Reflectance Changes Associated with Autumn Senescence of Aesculus hippocastanum L. and Acer platanoides L. Leaves. Spectral Features and Relation to Chlorophyll Estimation. Journal of Plant Physiology, **143** (3), 286-292, https://oi.org/10.1016/S0176-1617(11)81633-0.

GITELSON, A. A., GRITZ, Y. & MERZLYAK, M. N., 2003: Relationships between leaf chlorophyll content and spectral reflectance and algorithms for non-destructive chlorophyll assessment in higher plant leaves. Journal of Plant Physiology, **160** (3), 271-282, https://oi.org/10.1078/0176-1617-00887.

GOLDMAN, D. B., 2010: Vignette and exposure calibration and compensation. IEEE transactions on pattern analysis and machine intelligence, **32**(12), 2276-2288, https://oi.org/10.1109/TPAMI.2010.55.

HEIDARIAN DEHKORDI, R., BURGEON, V., FOUCHE, J., PLACENCIA GOMEZ, E., CORNELIS, J.-T., NGUYEN, F. et al., 2020a: Using UAV Collected RGB and Multispectral Images to Evaluate Winter Wheat Performance across a Site Characterized by Century-Old Biochar Patches in Belgium. Remote Sensing, **12**(15), 2504, https://oi.org/10.3390/rs12152504.

HEIDARIAN DEHKORDI, R., DENIS, A., FOUCHE, J., BURGEON, V., CORNELIS, J. THOMAS, TYCHON, B. et al., 2020b: Remotely-sensed assessment of the impact of century-old biochar on chicory crop growth using high-resolution UAV-based imagery. International Journal of Applied Earth Observation and Geoinformation, **91**, 102147, https://oi.org/10.1016/j.jag.2020.102147.

JEFFERY, S., VERHEIJEN, F., VAN DER VELDE, M. & BASTOS, A. C., 2011: A quantitative review of the effects of biochar application to soils on crop productivity using meta-analysis. Agriculture, Ecosystems & Environment, **144**(1), 175-187, https://oi.org/10.1016/j.agee.2011.08.015.

LI, M., SHAMSHIRI, R. R., WELTZIEN, C. & SCHIRRMANN, M., 2022: Crop Monitoring Using Sentinel-2 and UAV Multispectral Imagery: A Comparison Case Study in Northeastern Germany. Remote Sensing, **14**(17), 4426, https://oi.org/10.3390/rs14174426.

LIMA-CUETO, F. J., BLANCO-SEPÚLVEDA, R., GÓMEZ-MORENO, M. L. & GALACHO-JIMÉNEZ, F. B., 2019: Using Vegetation Indices and a UAV Imaging Platform to Quantify the Density of Vegetation Ground Cover in Olive Groves (Olea Europaea L.) in Southern Spain. Remote Sensing, **11**(21), 2564, https://oi.org/10.3390/rs11212564.

MINAŘÍK, R., LANGHAMMER, J. & HANUŠ, J., 2019: Radiometric and Atmospheric Corrections of Multispectral μMCA Camera for UAV Spectroscopy. Remote Sensing, **11**(20), 2428, https://oi.org/10.3390/rs11202428.

NANDA, A., MOHAPATRA, B. BHUSAN, MAHAPATRA, A. PRASADA KUMAR, MAHAPATRA, A. PRASAD KUMAR & MAHAPATRA, A. PRASAD KUMAR, 2021: Multiple comparison test by Tukey's honestly significant difference (HSD): Do the confident level control type I error. Int. J. Stat. Appl. Math., **6**(1), 59-65, https://oi.org/10.22271/maths.2021.v6.i1a.636.

RAMTEKE, I. K., RAJANKAR, P. B., OBI REDDY, G. P., KOLTE, D. M. & SEN, T. K., 2020: Optical remote sensing applications in crop mapping and acreage estimation: A review **2**(4).

SISHODIA, R. P., RAY, R. L. & SINGH, S. K., 2020: Applications of Remote Sensing in Precision Agriculture: A Review. Remote Sensing, **12**(19), 3136, https://oi.org/10.3390/rs12193136.

SMITH, G. M. & MILTON, E. J., 1999: The use of the empirical line method to calibrate remotely sensed data to reflectance. International Journal of Remote Sensing, **20** (13), 2653-2662, https://oi.org/10.1080/014311699211994.

TRUPIANO, D., COCOZZA, C., BARONTI, S., AMENDOLA, C., VACCARI, F. PRIMO, LUSTRATO, G. et al., 2017: The Effects of Biochar and Its Combination with Compost on Lettuce (Lactuca sativa L.) Growth, Soil Properties, and Soil Microbial Activity and Abundance. In International Journal of Agronomy, 1-12, https://oi.org/10.1155/2017/3158207.

VINCINI, M., FRAZZI, E. & D'ALESSIO, P., 2008: A broad-band leaf chlorophyll vegetation index at the canopy scale. Precision Agric, **9**(5), 303-319, https://oi.org/10.1007/s11119-008-9075-z.

YAO, H., QIN, R. & CHEN, X., 2019: Unmanned Aerial Vehicle for Remote Sensing Applications - A review. Remote Sensing, **11** (12), 1443, https://oi.org/10.3390/rs11121443.

ZHANG, X., FRIEDL, M. A. & SCHAAF, C. B., 2006: Global vegetation phenology from Moderate Resolution Imaging Spectroradiometer (MODIS): Evaluation of global patterns and comparison with in situ measurements. J. Geophys. Res., **111**(G4), https://oi.org/10.1029/2006JG000217.